

Fabrication and extreme micromechanics of additive metal microarchitectures

Sung-Gyu Kang ^{a, b*}, Bárbara Bellón ^a, Lalithkumar Bhaskar ^a, Siyuan Zhang ^a, Alexander Götz ^c, Janis Wirth ^c, Benjamin Apeleo Zubiri ^c, Szilvia Kalácska ^{d, e}, Manish Jain ^d, Amit Sharma ^d, Wabe Koelmans ^f, Giorgio Ercolano ^f, Erdmann Spiecker ^c, Johann Michler ^d, Jakob Schwiedrzik ^d, Gerhard Dehm ^a, and Rajaprakash Ramachandramoorthy ^{a*}

^a Max-Planck-Institut für Eisenforschung GmbH, Max-Planck-Straße 1, 40237 Düsseldorf, Germany

^b Current address: Department of Materials Engineering and Convergence Technology, Gyeongsang National University, Jinju-daero 501, 52828 Jinju, Republic of Korea

^c Department of Materials Science and Engineering, Institute of Micro- and Nanostructure Research, and Center for Nanoanalysis and Electron Microscopy (CENEM), Friedrich-Alexander-Universität Erlangen-Nürnberg, IZNF, Cauerstraße 3, Erlangen 91058, Germany

^d Empa, Swiss Federal Laboratories for Materials Science and Technology, Laboratory for Mechanics of Materials and Nanostructures, Feuerwerkerstrasse 39, 3602 Thun, Switzerland

^e Current address: Mines Saint-Etienne, Univ Lyon, CNRS, UMR 5307 LGF, Centre SMS, 158 cours Fauriel, Saint-Étienne, 42023, France

^f Exaddon AG, Sägereistrasse 25, Glattbrugg 8152, Switzerland

*Corresponding author: Dr. Sung-Gyu Kang and Dr. Rajaprakash Ramachandramoorthy

E-mail: s.kang@gnu.ac.kr and r.ram@mpie.de

Abstract

Metal microarchitectures with 3-dimensional solid frames can exhibit mechanical performance coming from the geometrical effect and characteristic size effect of material under dynamic and extreme temperature conditions. In this study, for the first time, full-metal Cu microlattices were fabricated via localized electrodeposition in liquid (LEL) process which enables high-precision additive manufacturing of metal at micro-scale. The microlattices possess a unique microstructure with micron sized grains that are rich with randomly oriented growth twins. They also have smooth surfaces and near-ideal nodal connectivity. Furthermore, Cu microlattices exhibited unique temperature (-150 and 25 °C) and strain rate (0.001–100 s⁻¹) dependent deformation behavior during *in situ* micromechanical testing. Systematic compression test of fully dense Cu micropillars, equivalent in diameter and length to the strut of microlattice at comparable extreme loading conditions, and post-mortem microstructural analysis revealed substantial shifts in deformation mechanisms depending on the temperature and strain rate. On one hand, at room temperature (25 °C), dislocation slip based plastic deformation occurs and leads to localized deformation of micropillars. On the other hand, at cryogenic temperature (-150 °C), mechanical twinning occurs and leads to relatively homogeneous deformation of micropillars. Based on the intrinsic deformation mechanisms at the component level, the temperature and strain rate dependent deformation behavior of microlattices is explained. Our findings provide valuable insights into the intricate mechanical responses and potential applications of metallic microarchitectures under dynamic and extreme temperature conditions.

1. Introduction

Mechanical metamaterials, characterized by their specialized 3-dimensional designs, exhibit exceptional physical and mechanical properties due to their intricate geometries, often inspired by nature¹, origami/kirigami^{2,3}, and atomic structures^{4,5}. Initially, the exploration of these architectures' properties was primarily conducted through computational approaches. However, advancements in additive manufacturing have enabled the realization of these three-dimensional architectures with elaborate geometries, allowing for greater design freedom. It has been observed that metallic architectures, capable of undergoing plastic deformation, exhibit superior mechanical properties and energy absorption capabilities under external loadings compared to their polymer or ceramic counterparts⁶⁻¹⁰. The characteristic deformation behavior of these metallic architectures positions them as prime candidates for damage protection in applications subjected to extreme loading conditions, such as aerospace components^{11,12} and biomaterials¹³⁻¹⁵. In this regard, the miniaturization of these 3-dimensional metallic architectures is expected to be a major advance in design and fabrication of future metal micro-electromechanical systems (MEMS), light weight packaging and protection of microelectronics against impacts, and micro-scale components of aviation and space applications.

Conventional powder- and energy deposition-based additive manufacturing processes face limitations in fabricating mesoscale architectures with a component size scale below 50 μm . Instead, microfabrication of 2.5-dimensional microarchitecture is optimized via widely known ultraviolet (UV) based lithographic method. Few studies have reported additive manufacturing of 3-dimensional metallic architectures at the mesoscale. Techniques such as direct ink writing¹⁶, laser-induced forward transfer¹⁷, laser-induced photoreduction¹⁸, and electrohydrodynamic redox¹⁹ have been deployed to fabricate metallic microarchitectures, but primarily with simpler geometries such as dots, pillars, and bridges. Furthermore, the simple microarchitectures in those studies show rough surfaces and internal porosities. Recently, hydrogen infusion-based additive manufacturing²⁰ has been used to fabricate more complex Ni architectures at nano- and micro-scales. As-fabricated Ni architectures showed complex geometries consistent with the original design, but showed rough surface and internal nanopores. Two-photon lithography (TPL) is extensively used to create templates for microarchitecture, which are subsequently filled through electrodeposition²¹. Cu²² and Ni microlattices^{23,24} with complex geometries fabricated by TPL and electrodeposition show smooth surfaces and good nodal connectivity. Expectedly, these microarchitectures exhibit

improved yield strengths due to the mechanical size effect of materials. However, the TPL based fabrication process is a complex two-step process and does not ensure 3-dimensional free-form metal architectures in mesoscale. During the electroplating into template, pores can be introduced to the deposited material due to hydrogen bubbles which are side-products of the process. Also, the surface can be irregular due to convection and electrolyte tapping during the electrodeposition. Lastly, struts of the microlattices in the previous studies showed elliptical cross-sections originating from TPL. Accordingly, the fabrication of 3-dimensional metallic microarchitecture has not been fully achieved and their deformation behavior and mechanical properties under extreme conditions which may result from the combined influence of geometrical and mechanical size effect are largely unexplored.

This study presents a pioneering approach in fabricating Cu microarchitectures using a localized electrodeposition in liquid (LEL) process, enabling high-precision creation of structures with component sizes ranging from a few microns to hundreds of microns (Figure 1(a)). LEL is a single-step fabrication technique that enables the consistent manufacture of full-metal 3D microarchitectures with complex geometries. As a model study, the structural and microstructural investigations were conducted on Cu microlattice with an octet geometry. Furthermore, to explore the mechanical performance under extreme conditions, *in situ* mechanical tests of the Cu microlattice were performed at a wide range of strain rates from 0.001 to 100 s⁻¹ and various temperature conditions (-150 and 25 °C). To elaborate on the unique deformation behavior and the mechanical performance of the microlattice, Cu micropillars with the same size scale as the microlattice's strut were fabricated and mechanically tested under the same conditions. The pre- and post-mortem structural and microstructural analysis of Cu micropillar explains the deformation behavior of the microlattice. The results demonstrate the feasibility of fabricating three-dimensional free-form metal architectures at the micron scale and consequently, highlighting the superior mechanical properties under extreme loading conditions, enabled by the combination of intrinsic and extrinsic size effects.

2. Results and discussion

Microlattice of this study

We chose the octet truss design, which is known for its low mass density and good structural rigidity originating from its high nodal connectivity, as the unit-cell geometry. The unit-cell length and the strut diameter were chosen as 15 μm and 2.5 μm , respectively. The microlattice was constructed by repeating the unit cell three times along each coordinate axis (Figure 1(b)). To ensure uniform deformation along the loading direction, the 5- μm -thick plates were added at the bottom and top of the lattice structure. Figure 1(c) shows location of each voxels for actual printing. The diameter of voxel and overlap between voxels were set as 2.5 μm and 0.5 μm , respectively. Figure 1(d) shows an SEM image of an as-fabricated Cu microlattice. Clearly, the printed microlattice shows straight struts and a smooth surface, which is consistent with the original computer aided design (CAD) model. The quality of microlattices is different from the microlattices in previous studies that used the two-step processes^{20,22–24}. It can be attributed to the printing manner of localized electrodeposition, optimized printing parameters, and the additives, such as levelers and grain refiners, in electrochemical ink (detailed information is available in the Methods section). Firstly, the electrodeposition is done in a voxel-by-voxel manner and the voxel print location is controlled by programmable piezos with nanometer precision, which enables voxelized printing of Cu at a precise location. Secondly, the printing parameters for the microlattice in this study were optimized. It was observed that the nodal connectivity and strut diameter are highly dependent on the printing parameters such as the potential for the printing chamber and pressure for ion ink flow (Figure S1). Through trial and error, the optimal potential (-0.5 V) and pressure (25 mbar) were found. Lastly, the additives in the electrochemical ink lead to a smooth and consistent surface of the microlattice and consistent microstructure throughout the architecture. The dimples at the top plate are possibly originated from the skipped voxels during electrodeposition. To examine the pore channel of the lattice and internal defect in the material that these skipped voxels can cause, we conducted NanoCT. Figure 1(e) is the 3D reconstruction of the microlattice. As expected from SEM images, the microlattice structure and the representative unit cell are consistent with the original design in Figure 1(b). Moreover, it demonstrates the micron-scale resolution and geometric freedom of the LEL process. Figure 1(f) shows the diameters of arbitrarily chosen 70 struts (measured at the center). The average strut diameter is $2.52 \pm 0.11 \mu\text{m}$, and the relative density is about 0.28.

Figure 1(g, h) shows the microstructure of the representative unit cross-section along the building direction of the microlattice obtained using SEM-TKD. The unindexed areas that can be observed at the node and corners of struts may be originated from the ion-beam milling-induced damage. Both inverse pole figure maps (Figure 1(g)) along and perpendicular to the building direction explain that the microlattice consists of polycrystalline Cu without strong crystallographic texture. In the GB map (Figure 1(h)), high-angle grain boundaries (colored in blue) show that there are 2–3 grains across the strut diameter (average grain size of $1.04 \pm 0.24 \mu\text{m}$). Importantly, there is a high fraction of $\Sigma 3$ twin boundaries within the grain. The color of the twin boundary was set to gradually change from yellow to red, as the misorientation angle moves away from 60° to 50° . Apparently, for the twin boundaries in the as-fabricated microlattice, the misorientation angle between neighboring grains is almost 60° . The formation of twin boundaries during LEL may be attributed to the additives, as they increase the nucleation sites of Cu deposition and reduce the interfacial energy, leading to the formation of twin boundaries²⁵. In summary, the Cu microlattice in this study shows well-defined geometry and dense microstructure with a high fraction of twin boundaries.

Compression of microlattices

To examine the deformation behavior and mechanical performance of Cu microlattice, *in situ* micromechanical tests were performed under various extreme conditions. Using a piezo-based actuator with an embedded strain gage for measuring displacement and a typical strain gauge-based load cell, the mechanical response of the microlattices was captured at both room and cryogenic temperatures at strain rates ($\dot{\epsilon}$) of 0.001 till 1 s^{-1} . At room temperature, the rate-dependent properties of the microlattices were further captured at higher strain rates up to 100 s^{-1} via a high-stiffness piezoelectric load cell, replacing the compliant strain gauge-based load cell. Note that this is the first systematic study on the deformation behavior of metallic microlattices under extreme conditions with strain rates spanning 5 magnitudes and cryogenic temperatures. The only accessible previous study reported a compression testing of polymer microlattices at $\dot{\epsilon}$ of 1000 s^{-1} and room temperature²⁶. A flat punch indenter with a diameter of $150 \mu\text{m}$ was used. Detailed information on mechanical testing systems is given elsewhere²⁷. Figure 2(a, b) shows SEM images of the microlattices during compression at a $\dot{\epsilon}$ of 0.01 s^{-1} at both room temperature (RT) and cryogenic temperature (CT). Regardless of temperature, the microlattice seems to exhibit homogeneous deformation overall, but the struts of the microlattice show slightly different deformation behavior depending on temperature. At RT,

the deformation starts with the buckling of struts at the bottom plate (indicated by white arrows). It was reported that the deformation of the lattice starts from the struts with low nodal connectivity, that is, the struts at the surface or corner²⁸. At CT, on the other hand, there was no noticeable buckling of surface or corner struts. Figure 2(c) shows the representative stress-strain curves of microlattices compressed at different temperatures and different $\dot{\epsilon}$ conditions (2-3 microlattices were tested at each condition). The microlattice shows higher yield strength (and flow stress at 0.2 engineering strain - Figure S2) at CT than RT as plotted in Figure 2(d), which may also be attributed to the buckling of struts. The buckling of struts can be captured by a stress overshoot after the elastic deformation in the stress-strain curve. The curves in the insets obtained at 0.001, 0.01, and 0.1 s⁻¹ clearly show that the stress overshoot occurred only at RT. In addition, as shown in Figure 2(c) (and more in detail in Figure S3), except for the microlattice compressed at 100 s⁻¹, all microlattices compressed at RT exhibit the stress overshoot after the elastic deformation in the stress-strain curves, while those compressed at CT do not. This stress overshoot, also known as post-yield softening, is known to occur in the lattice structure due to an abrupt buckling or fracture of struts^{29,30}. Oscillations are observed in the stress-strain curve at RT 100 s⁻¹ beyond yield. This ringing can be induced by the change in the stiffness of the sample (for example at the elastic-plastic transition) during deformation at high $\dot{\epsilon}$ ³¹.

A clear rate-dependency can be seen from the stress-strain signatures of the microlattices. For example, at RT, the yield strength in Figure 2(d) increases with $\dot{\epsilon}$ until ~ 1 s⁻¹ (107.09 \pm 7.34 MPa at 0.001 s⁻¹ and 160.76 \pm 2.57 MPa at 1 s⁻¹). Beyond a $\dot{\epsilon}$ of 1 s⁻¹, the yield strength almost saturates. At CT, on the other hand, yield strength shows negligible change with $\dot{\epsilon}$ from 0.001 to 1 s⁻¹ and is almost constant at around 230 MPa. The rate sensitivity factor was extracted based on Eq. (1) below:

$$m = \frac{\partial \ln \sigma}{\partial \ln \dot{\epsilon}} \quad (1)$$

where σ is yield strength. At RT, the microlattice shows m value of 0.0516 \pm 0.0078 up to a $\dot{\epsilon}$ of 1 s⁻¹ and then shows a decreased value of 0.0004 \pm 0.0008 up to a $\dot{\epsilon}$ of 100 s⁻¹. At CT, the microlattice shows a low m value of 0.0015 \pm 0.0017 up to a $\dot{\epsilon}$ of 1 s⁻¹. Different m values suggest that the deformation mechanism of microlattice changes with temperature and $\dot{\epsilon}$.

Change in the deformation mechanism of microlattice can also be confirmed via the compressed shape. Figure 2(e, f) shows the compressed SEM images of microlattices. At RT (Figure 2(e)), the struts at the surface of the microlattice bulged out perpendicular to the loading

direction at high $\dot{\varepsilon}$ ($\geq 1 \text{ s}^{-1}$). At CT (Figure 2(f)), on the other hand, the bulging out of the surface struts occurred regardless of $\dot{\varepsilon}$. The degree of bulging out has been calculated (Figure S4) and shows a clear $\dot{\varepsilon}$ and temperature dependencies, which mimics closely the dependencies in the yield strength (Figure 2(d)). Moreover, compared to the struts before compression in Figure 1(c), the struts of microlattices after the compression at RT show clear slip steps as indicated by the white arrows in Figure 2(e). The slip steps are easier to find in the microlattices compressed at rather low $\dot{\varepsilon}$, suggesting less localized deformation of the strut at high $\dot{\varepsilon}$ ($> 1 \text{ s}^{-1}$). In the case of the struts of microlattices compressed at CT, they show smoother surfaces and thicker diameters, indicating more homogeneous deformation of struts at CT than RT. The above analysis on the yield strength, the degree of bulging out, and the slip steps at the struts of compressed microlattices suggest that the deformation behavior of microlattices in this study can be categorized into three regimes: RT 0.001–1 s^{-1} , RT 1–100 s^{-1} , and CT 0.001–1 s^{-1} .

Figure 2(g) shows the absorbed energy of the microlattices with respect to density and compares it against the absorbed energies of other microlattices previously reported in the literature. The absorbed energy (U_A) can be obtained as below:

$$U_A = \int_0^{\varepsilon_d} \sigma d\varepsilon \quad (2)$$

where the σ , ε , and ε_d are the stress, strain, and densification strain, respectively. For simplicity, U_A of microlattices compressed at RT 0.001, 1, 100 s^{-1} and CT 0.001, 1 s^{-1} are plotted in Figure 2(g). The U_A of microlattices is 1.5~2.0 times higher at CT than RT, as expected from the stress-strain curves in Figure 2(c). Importantly, compared to the Cu microlattice from a previous study²², the microlattices in this study show comparable U_A even with lower relative density. It can be attributed to the microstructure, the geometry of the strut, and the nodal connectivity in the microlattices used in our current study. First, due to the small grain size, and a large number of twin and grain boundaries in the microlattices of this study, high yield strength and strong hardening behavior during deformation are expected. Second, the microlattice in this study shows a nearly circular cross-section of the strut, which is not the case in the previous study of Gu et al²². A strut with a circular cross-section would lead to relatively even stress distribution at the strut-node intersection during deformation compared to that with an elliptical cross-section. Finally, the nodal connectivity which is close to the original design would lead to high strength and high energy absorption capability of the microlattice. To investigate the effect of nodal connectivity, we conducted an additional compression test of Cu microlattice with poor connectivity (Figure S5) and the deformation is concentrated in the node, leading to a localized fracture. The corresponding yield and flow

stresses are only a quarter of those of the microlattices with good nodal connectivity. Further, to determine whether the existence of a top plate affects the deformation behavior and also U_A , finite element methods (FEM) based simulations were conducted. The compressive load-displacement curves of microlattices with and without the top plate show no significant difference (Figure S6). Accordingly, the Cu microlattice structures in this study exhibit superior mechanical properties compared to the previous study of Gu et al, due to their unique microstructure and precise geometry that is near-identical to the original CAD model²². Similar reasoning can be used to explain the fact that the Cu microlattices in this study can achieve an energy absorption per unit mass of 20 J/g, which is comparable to or significantly better than the microlattices made of other metals (Aluminum, Nickel³², and Gold³³), polymer³⁴, metal-polymer composite^{35,36}, pyrolyzed carbon³⁷, and alumina³⁸ etc.

Base material characterization – Copper micropillar compression

In order to understand better the deformation mechanisms of the microlattice, the base material Cu with the same microstructure was characterized using micropillar compression at similar rates and temperatures. It should be noted that a FEM simulation confirmed that the global strain rate experienced by the microlattices is quite analogous to the strain rate locally in the struts and nodes (except for at the struts in the very surface – Figure S7).

The Cu micropillars were also fabricated by LEL. Figure 3(a, b) shows a computer-aided design and voxel locations of the dog-bone-shaped micropillar with a diameter of 3 μm and a length of 10 μm in a gauge section, ably mimicking the dimensions of the struts used in the microlattices. Via the LEL process, arrays of micropillars ($20 \times 22 = 440$ pillars) were fabricated on the substrate. As-fabricated micropillars show a smooth surface and a straight gauge section which are again consistent with the original CAD model (Figure 3(c)).

For microstructural analysis, the cross-section of the micropillar parallel to the loading direction was sampled via focused ion beam milling. Figure 3(d) shows the inverse pole figure (IPF) maps along and perpendicular to the building direction and the grain boundary (GB) map of the gauge section of the as-built micropillar obtained using TKD. The IPF map indicates the Cu micropillar is indeed polycrystalline and the GB map, high-angle grain boundaries (colored in blue) explain that there are 2~3 grains across the pillar diameter, which is consistent with the strut of the microlattices. Importantly, a high fraction of $\Sigma 3$ boundaries were also present in the grains and their misorientation angle distribution was similar to those present in the microlattices (Figure S8), confirming the similarity of microstructure between them. Via an *in*

situ micromechanical testing system with the same piezo-based actuator used for testing the microlattices, compression tests were conducted at room/cryogenic temperatures and a wide range of $\dot{\epsilon}$.

When the temperature changes, Cu micropillars also show different deformation behavior. Figure 3(e) shows the stress-strain curves of micropillars. The curves show higher yield strength and flow stress at CT than at RT. Figure 3(f) shows the summary of yield strength of Cu micropillars at different $\dot{\epsilon}$ and temperatures. Depending on $\dot{\epsilon}$, the yield strength is 1.1–1.4 times higher at CT than at RT. Moreover, at RT the yield strength increases with $\dot{\epsilon}$ when $\dot{\epsilon} \leq 1 \text{ s}^{-1}$. When $\dot{\epsilon} > 1 \text{ s}^{-1}$, there is no noticeable change in the stress-strain curves with $\dot{\epsilon}$. As shown in Figure 3(g), analogous to the microlattice, the micropillars compressed at RT and $\dot{\epsilon} \leq 1 \text{ s}^{-1}$ exhibit m value of 0.0312 ± 0.0016 , while at $\dot{\epsilon} > 1 \text{ s}^{-1}$, the micropillars exhibit a significantly low m value of 0.0008 ± 0.0003 . At CT, the micropillars exhibit a low m value of 0.0048 ± 0.0015 regardless of the value of $\dot{\epsilon}$. A similar trend was found in the flow stress obtained at engineering strain of 0.2 (Figure S9). Lastly, there are stress drops in the stress-strain curves of micropillars compressed at CT 0.001, 0.01, 0.1 s^{-1} . The stress drop at CT will be discussed in detail in the following section.

The compressed shape (Figure 3(g) and S10) of the micropillars also suggests changes in the deformation behavior at different rates and temperatures. At RT, when $\dot{\epsilon} \leq 1 \text{ s}^{-1}$ the compressed micropillars show clear slip steps on the surface, suggesting a localized deformation. When $\dot{\epsilon} \geq 1 \text{ s}^{-1}$, the micropillars exhibit a mixed mode deformation, where not only slip steps appear on the surface but also partial barreling-like homogeneous deformation around the slip step. At CT, regardless of $\dot{\epsilon}$, the compressed micropillars show relatively homogeneous deformation without any localized slip step on the surface. The clues to the deformation mechanism behind can be obtained using post-mortem microstructural analysis. The cross-sections of compressed micropillars parallel to the loading direction were sampled via focused-ion beam milling.

Temperature and rate responsive deformation mechanism of Cu micropillars

Compression leads to major changes in the microstructure of the micropillars. Figure 4(a) shows the IPF map along the building direction and the GB map of the gauge section of the micropillar compressed at RT and $\dot{\epsilon}$ of 0.001, 1, and 100 s^{-1} . In every case, the straight growth twin boundaries appear to decrease after the compression. The GB maps indicate increased high-angle grain boundaries and defective twin boundaries in the gauge section of the

compressed micropillars. Here, the defective twin boundary is the twin boundary where the misorientation angle between neighboring grains deviates from 60° .

Change in the microstructure can be attributed to the interaction between the moving dislocations and the twin boundaries. It was reported that either cross slip or transmission of partial dislocations at the twin boundary results in the formation of a stair-rod dislocation and a Shockley partial dislocation on the twin boundary³⁹⁻⁴². A Shockley partial dislocation moves along the twin boundary and leaves a step on the twin boundary, resulting in a deviation of misorientation angle at the twin boundary⁴⁰. Further deformation introduces more Shockley partial dislocations on the twin boundary and their movement leads to de-twinning^{43,44}. Once the de-twinning is finished, a large number of stair-rod dislocations remain. These sessile dislocations impede further dislocation movement and progressively may transform the area into a grain boundary. Notably, the region with increased high-angle grain boundary and the defective twin boundary is wider in the micropillar compressed at RT and $\dot{\epsilon} = 100 \text{ s}^{-1}$ than $\dot{\epsilon} = 0.001$ and 1 s^{-1} . It suggests that at $\dot{\epsilon} = 100 \text{ s}^{-1}$ the deformation is relatively homogeneous throughout the gauge section of the micropillar, which is consistent with the SEM image in Figure 3(g).

Figure 4(b) shows the IPF map along the building direction and the GB map of the gauge section of the micropillar compressed at CT and $\dot{\epsilon} = 0.001$ and 1 s^{-1} . The microstructures of micropillars commonly show increased high-angle grain boundaries. What should be noted is that there are straight defective twin boundaries in the GB maps. In the case of the micropillar compressed at CT and $\dot{\epsilon} = 0.001 \text{ s}^{-1}$, these twin boundaries are located at the center and upper part of the gauge section. In the case of the micropillar compressed at CT and $\dot{\epsilon} = 1 \text{ s}^{-1}$, these twin boundaries are mostly found in the right part of the pillar. Moreover, the width between these straight twin boundaries is narrower than that between the growth twin boundaries in Figure 3(d), suggesting newly formed deformation twin boundaries.

TEM analysis provided the high-resolution microstructure analysis which is difficult to obtain from SEM-TKD analysis. Figure 4(c) shows the TEM images of the micropillar compressed at CT and $\dot{\epsilon} = 0.001 \text{ s}^{-1}$. We specifically focused on the gauge section with straight boundaries. Diffraction patterns obtained from selected areas with straight twin boundaries (Area 1 and 2) clearly indicate that the straight boundaries are the deformation twin boundaries with $(\bar{1}\bar{1}1)$ twin plane, suggesting that the mechanical twinning occurred in the micropillar during compression at CT. Notably, unlike the deformation twin boundaries in TEM images, some twin boundaries in SEM-TKD images are perpendicular to the loading direction (Figure

4(b)). It can simply be attributed to the sampling direction. Pole figure analysis, further confirmed that these twin boundaries are not perpendicular to the loading direction but have a $\sim 30^\circ$ angle (Figure S11). Figure 4(d) summarizes the microstructural changes in the compressed micropillars especially focused on the misorientation angle distribution. The non-compressed micropillar shows high fraction of $\Sigma 3$ boundary (at misorientation of 60°). With tolerance of 5° , the $\Sigma 3$ boundary fraction of non-compressed micropillar is about 0.86. After deformation at RT, the $\Sigma 3$ boundary fraction of micropillar decreases (0.61 and 0.59 when compressed at 0.001 and 1 s^{-1} , respectively). After deformation at CT, the $\Sigma 3$ boundary fraction of micropillar decreases, but less than at RT (0.73 and 0.71 when compressed at 0.001 and 1 s^{-1} , respectively), suggesting that the mechanical twinning dominates during deformation at CT. Combined with the microstructural analysis, the stress drop event occurred only at CT in Figure 3(e) is a typical signature of mechanical twinning involved deformation mechanism. It has been previously reported that the mechanical twin can occur in the Cu when deformed at CT and lead to stress drops^{45,46}. Figure 4(e) shows stress drop magnitudes ($\Delta\sigma$) and drop times (Δt) from the stress-strain curves. The inset plot explains, as an example, how $\Delta\sigma$ and Δt were evaluated from the stress-strain curve at CT 0.01 s^{-1} . Clearly, except for a few outliers, most data points are located in the range of $23 < \Delta\sigma < 80 \text{ MPa}$ and $0.075 < \Delta t < 0.35 \text{ s}$, suggesting that the stress drop may be induced by the same event. Given the drop time, it can be deduced that at $\dot{\epsilon} = 1 \text{ s}^{-1}$ the stress drop is less likely to occur because the total deformation time is relatively short (about 0.2 s). Meyers *et al.* previously suggested that a slip-to-twin transition can occur at low temperatures as the stress for dislocation slip increases with decreasing temperature.

Figure 4(f) exhibits the postulated deformation mechanism of Cu micropillar at various temperatures and $\dot{\epsilon}$. At RT $0.001\text{--}1 \text{ s}^{-1}$, a dislocation may glide, leading to localized deformation and the slip step at the surface⁴⁷. During the dislocation glide, the dislocation-twin boundary interaction most probably occurs. The apparent activation volume (V^*), a kinetic signature of the deformation mechanism, can be obtained from Eq. (3) below:

$$V^* = \sqrt{3}k_B T \frac{\partial \ln \dot{\epsilon}}{\partial \sigma} \quad (3)$$

where k_B is the Boltzmann constant and T is the temperature. With the Burgers vector \mathbf{b} of 0.255 nm for a perfect dislocation of Cu, V^* of Cu micropillar at RT $0.001\text{--}1 \text{ s}^{-1}$ is $34.35 \pm 2.03 \text{ b}^3$ corresponding typically to dislocation-twin boundary interaction^{48–50}. At RT $1\text{--}100 \text{ s}^{-1}$, we hypothesize that the applied stress is already high, and multiple dislocations can move simultaneously, leading to enhanced interactions between them. These dislocation movements

may lead to dislocation-twin boundary interaction that occurs throughout the pillar^{51,52}. The corresponding hardening modulus of micropillars at RT in Figure S12 shows a constant increase with strain rate, which can be attributed to the increased number of dislocation movement. As such, compared to the low $\dot{\epsilon}$, the deformation is relatively homogeneous, but the dislocation glide can still occur and leave slip steps at the surface. This is also reflected in the apparent activation volume calculated in this regime ($958.85 \pm 190.83 \text{ b}^3$) and it is quite close to the value for a typical forest dislocation movement. At CT $0.001\text{--}1 \text{ s}^{-1}$, mechanical twinning may occur at multiple grains (activation volume of $72.95 \pm 21.92 \text{ b}^3$) due to the low temperature and high stress involved, leading to homogeneous deformation without any slip steps at the surface. The corresponding hardening modulus at CT shows relatively constant values regardless of the strain rate increase.

Deformation behavior of microlattice based on micro-pillar properties

Finally, the deformation behavior of the microlattice can be elucidated from the viewpoint of the micropillar's deformation mechanism. A difference in the relative strength at RT and CT can be attributed to the global mechanical response of microlattice under compression originating from the intrinsic deformation mechanisms at the component level, that is, the strut. During the initial deformation, the struts at the outer surfaces are prone to deform first due to less nodal connectivity. We hypothesize that, at CT, the plastic deformation is governed by mechanical twinning in multiple grains, leading to homogeneous deformation of the strut without introducing any mechanical instabilities as shown in Figure 2(e). On the other hand, at RT, the plastic deformation governed by dislocation nucleation and slip is expected, leading to relatively localized deformation of struts and slip steps at the surface.

The localized deformation can act as a mechanical instability during deformation and further lead to buckling deformation of the strut, which is already confirmed by the stress overshoot in the stress-strain curves. The critical buckling strength (σ_{cr}) of the strut can be estimated from the Euler buckling theory as follows:

$$\sigma_{cr} = \frac{\pi^2 E}{4} \left(\frac{R}{L}\right)^2 \quad (4)$$

where E is Young's modulus (110 GPa for Cu), R is the radius of the strut, and L is the length of the strut. Eqn. (4) gives σ_{cr} of 603 MPa which is higher than the yield strength of Cu micropillars at any $\dot{\epsilon}$ and temperature, suggesting that the buckling of the strut in the microlattice is not favorable during compression. However, it should be noted that an

introduction of surface imperfections is known to lower σ_{cr} ⁵³⁻⁵⁵. Ranjbartoreh and Wang reported that topological defects decrease σ_{cr} of carbon nanotube by 30 %⁵⁵. From this perspective, a rough estimate of σ_{cr} of a strut with a slip step at the surface is about 422 MPa, which is comparable to the yield strength of the Cu micropillar at RT. A dynamic increase factor (DIF, $\sigma_{dynamic}/\sigma_{quasi-static}$) indirectly supports the proposed deformation mechanism of microlattice (for reference see Figure S13. The DIFs of microlattice and micropillar show negligible difference at CT. On the other hand, the DIFs of microlattice and micropillar show a clear difference at RT, suggesting that the deformation behavior is different. In the micropillar, simple uniaxial compression leading to surface slip steps is expected. In the microlattice, buckling of the strut, which is facilitated by the surface slip steps, and subsequent stretch-dominated deformation is expected (as supported by Figure 2(e)). At CT, the compression leads to homogeneous deformation in the strut, leading to higher yield strength and flow strength compared to RT.

3. Conclusion

Cu microlattices were fabricated via the LEL process, with smooth surfaces and ideal nodal connectivity. These microlattices exhibited unique deformation behaviors dependent on temperature and strain rate during *in situ* micromechanical testing. A detailed study on the deformation mechanism of micropillars—having the same diameter and length as the struts of the microlattice revealed significant differences in the deformation mechanism based on temperature and strain rate. These distinct rate-and temperature-dependent deformation behaviors of the microlattice can be attributed to the collective mechanical response of the microlattice under compression, stemming from the intrinsic deformation mechanisms present at the component level, specifically the strut. This comprehensive understanding provides insights into the nuanced responses and functionalities of such metallic microstructures under demanding operational conditions.

Methods

Printing of microarchitectures

Cu microarchitectures in this study were fabricated by LEL via localized force-controlled electrodeposition using the CERES system (Exaddon AG, Switzerland). Copper (Cu) ions (0.5 M CuSO₄ in 51 mM H₂SO₄ and 0.48 mM HCl with brightener and leveler additives) flow through a 300-nm-diameter orifice in a silicon nitride AFM tip immersed in a standard three-cell electrochemical cell by applied pressure. Subsequently, the ions are deposited at desired locations on a Si/Ti (10 nm)/Cu (100 nm) substrate contacting the working electrode. The deposition is done in a voxel-by-voxel manner such that the AFM cantilever moves to the next voxel coordinate when it is deflected by the growing Cu voxel and the laser beam on top of the AFM cantilever senses the deflection. The deflection threshold is in the order of 1 nm. The pressure and applied potential of LEL for microlattice printing were 20 mbar and -0.5 V, respectively. For micropillar printing, the applied potential was -0.5 V, and the pressure was carefully controlled in the range of 20 ~ 70 mbar to obtain consistent diameter in the gauge section. To get smooth surfaces, the distance between each voxel was kept at 0.5 μm. Previous studies have already shown that the Cu parts printed via LEL show dense microstructure and smooth surfaces⁴⁷. Detailed information on LEL is given elsewhere⁵⁶.

Microstructural characterization

The microstructure of Cu microlattices and micropillars was characterized via SEM-TKD and STEM analysis. The cross-sections parallel to the deposition direction (along z-axis) were sampled using focused-ion-beam milling (Thermo Fisher Scios 2 dual beam FIB/SEM). TKD patterns were captured in a Zeiss Sigma SEM operated at 20 kV. A critical misorientation angle for grain boundaries was set as 15° to distinguish between low-angle grain boundary (LAGB) and high-angle grain boundary (HAGB). Twin boundaries were identified according to the rotation axes and angles, with a deviation tolerance of 5°. Scanning transmission electron microscopy (STEM) was conducted on a Titan Themis microscope operated at 300 kV. The convergence semi-angle of the aberration-corrected probe is 23.8 mrad to reach a probe size of 0.1 nm. High-angle annular dark field (HAADF) STEM images were taken using a detector range of 73~200 mrad. Energy-dispersive X-ray spectroscopy (EDS) was taken using a SuperX detector. The STEM-EDS spectrum imaging dataset was denoised by multivariate statistical before elemental quantification⁵⁷.

***in situ* micromechanical test**

The compression experiments were performed *in situ* using an Alemnis indenter (Alemnis AG, Switzerland). The tests at room temperature and low temperature were carried out using an Alemnis Standard Assembly (ASA) and an Almenis LTM-Cryo, respectively. To perform the *in situ* tests, the indenter was installed in a Zeiss Gemini 500 SEM (Zeiss, Germany) and a JEOL JSM-6490 (JEOL Instruments, Japan). Experiments were performed in both setups in displacement control using a flat punch diamond indenter of 150 μm diameter for the microlattices and 5 μm for the micropillars (Synton-MDP AG, Switzerland). The Alemnis indenter has a piezoelectric actuator that enables intrinsic displacement control and a strain gauge load cell that limits the actuation speeds to 10 $\mu\text{m/s}$ due to the ringing of the load cell. The Alemnis indenter incorporates a piezoelectric actuator that allows for precise intrinsic displacement control, but its actuation speed is limited to 10 $\mu\text{m/s}$ due to the load cell's susceptibility to ringing. With this specific setup, it's only possible to achieve strain rates up to 1/s. To enable strain rates beyond 1/s, a piezo-based load cell was employed instead of the strain gauge load cell, allowing for a maximum achievable speed of 10 mm/s. Given the short time scales of the experiments, data acquisition systems with a high-frequency capability of 1 MHz were utilized to record load and displacement data. Furthermore, to mitigate the impact of resonance on the load data, load measurements were taken both with and without the sample under identical input displacement conditions. Subsequently, the load specific to the sample, devoid of any resonance effects, was derived by subtracting the load recorded with the sample from the load recorded without the sample.

The LTM-Cryo setup consists of a cold finger that is cooled by liquid nitrogen, which is pumped into the system from an outside dewar²⁴. The cold finger is linked to the tip and the sample by Cu braids and separated from the indenter frame by ceramic shafts. The tip, sample, and frame have individual resistive heaters and thermocouples in a closed feedback loop that enable complete control of the temperature in the system. To minimize drift, we maintained the frame at a constant temperature using the aforementioned heaters and temperature feedback. Once the system was cooled down, we switched on the frame heaters and let them stabilize until the change in frame temperature was less than $\pm 0.01^\circ\text{C}$ in 10 minutes. Before performing actual compression on the microlattices, we matched the temperature between the indenter and the sample to eliminate drift⁵⁸. For this, we conducted several indentations under load control, where the indenter or sample temperature was changed with respect to the other by $\pm 5^\circ\text{C}$. We then measured the drift in a hold segment during the unload. We chose the pair of temperatures

that provided a drift lower than 100 pm/s. We repeat this procedure at the beginning of every set of tests.

References

1. Kumar Katiyar, N., Goel, G., Hawi, S. & Goel, S. Nature-inspired materials: Emerging trends and prospects. *NPG Asia Mater* **13:56**, (2021).
2. Chen, S., Chen, J., Zhang, X., Li, Z. Y. & Li, J. Kirigami/origami: unfolding the new regime of advanced 3D microfabrication/nanofabrication with “folding”. *Light: Science and Applications* vol. 9 Preprint at <https://doi.org/10.1038/s41377-020-0309-9> (2020).
3. Neville, R. M., Scarpa, F. & Pirrera, A. Shape morphing Kirigami mechanical metamaterials. *Sci Rep* **6:1**, 1–12 (2016).
4. Wu, Y. *et al.* Additively manufactured materials and structures: A state-of-the-art review on their mechanical characteristics and energy absorption. *Int J Mech Sci* **246**, 108102 (2023).
5. Riva, L., Ginestra, P. S. & Ceretti, E. Mechanical characterization and properties of laser-based powder bed-fused lattice structures: a review. *The International Journal of Advanced Manufacturing Technology* **113**, 649–671 (2021).
6. Choy, S. Y., Sun, C. N., Leong, K. F. & Wei, J. Compressive properties of functionally graded lattice structures manufactured by selective laser melting. *Mater Des* **131**, 112–120 (2017).
7. Zhao, Z. yu, Han, B., Wang, X., Zhang, Q. cheng & Lu, T. J. Out-of-plane compression of Ti-6Al-4V sandwich panels with corrugated channel cores. *Mater Des* **137**, 463–472 (2018).
8. Maskery, I. *et al.* A mechanical property evaluation of graded density Al-Si10-Mg lattice structures manufactured by selective laser melting. *Materials Science and Engineering: A* **670**, 264–274 (2016).
9. Lee, B. K. & Kang, K. J. A parametric study on compressive characteristics of Wire-woven bulk Kagome truss cores. *Compos Struct* **92**, 445–453 (2010).
10. Weeks, J. S., Gandhi, V. & Ravichandran, G. Shock compression behavior of stainless steel 316L octet-truss lattice structures. *Int J Impact Eng* **169**, 104324 (2022).
11. Bici, M. *et al.* Development of a multifunctional panel for aerospace use through SLM additive manufacturing. *Procedia CIRP* **67**, 215–220 (2018).
12. Zhou, J., Shrotriya, P. & Soboyejo, W. O. On the deformation of aluminum lattice block structures: from struts to structures. *Mechanics of Materials* **36**, 723–737 (2004).
13. Burton, H. E. *et al.* The design of additively manufactured lattices to increase the functionality of medical implants. *Materials Science and Engineering: C* **94**, 901–908 (2019).

14. Alabort, E., Barba, D. & Reed, R. C. Design of metallic bone by additive manufacturing. *Scr Mater* **164**, 110–114 (2019).
15. Feng, J., Liu, B., Lin, Z. & Fu, J. Isotropic octet-truss lattice structure design and anisotropy control strategies for implant application. *Mater Des* **203**, 109595 (2021).
16. Ahn, B. Y. *et al.* Omnidirectional Printing of Flexible, Stretchable, and Spanning Silver Microelectrodes. *Science (1979)* **323**, 1590–1593 (2009).
17. Makrygianni, M., Kalpyris, I., Boutopoulos, C. & Zergioti, I. Laser induced forward transfer of Ag nanoparticles ink deposition and characterization. *Appl Surf Sci* **297**, 40–44 (2014).
18. Ishikawa, A., Tanaka, T. & Kawata, S. Improvement in the reduction of silver ions in aqueous solution using two-photon sensitive dye. *Appl. Phys. Lett* **89**, 113102 (2006).
19. Men trety, M. *et al.* Targeted Additive Micromodulation of Grain Size in Nanocrystalline Copper Nanostructures by Electrohydrodynamic Redox 3D Printing. *Small* **18**, (2022).
20. Zhang, W. *et al.* Suppressed Size Effect in Nanopillars with Hierarchical Microstructures Enabled by Nanoscale Additive Manufacturing. *Nano Lett* **23**, 8162–8170 (2023).
21. Bernardeschi, I., Ilyas, M. & Beccai, L. A Review on Active 3D Microstructures via Direct Laser Lithography. *Advanced Intelligent Systems* **3**, 2100051 (2021).
22. Wendy Gu, X. & Greer, J. R. Ultra-strong architected Cu meso-lattices. *Extreme Mech Lett* **2**, 7–14 (2015).
23. Khaderi, S. N. *et al.* The indentation response of Nickel nano double gyroid lattices. *Extreme Mech Lett* **10**, 15–23 (2017).
24. Schwiedrzik, J. *et al.* Dynamic cryo-mechanical properties of additively manufactured nanocrystalline nickel 3D microarchitectures. *Mater Des* **220**, 110836 (2022).
25. Lin, C.-C. & Hu, C.-C. The Ultrahigh-Rate Growth of Nanotwinned Copper Induced by Thiol Organic Additives. *J Electrochem Soc* **167**, 082505 (2020).
26. Lai, C. Q. & Daraio, C. Highly porous microlattices as ultrathin and efficient impact absorbers. *Int J Impact Eng* **120**, 138–149 (2018).
27. Ramachandramoorthy, R. *et al.* High strain rate in situ micropillar compression of a Zr-based metallic glass. *J Mater Res* **36**, 2325–2336 (2021).
28. Jost, E. W., Moore, D. G. & Saldana, C. Evolution of global and local deformation in additively manufactured octet truss lattice structures. *Additive Manufacturing Letters* **1**, 100010 (2021).

29. Tancogne-Dejean, T., Spierings, A. B. & Mohr, D. Additively-manufactured metallic micro-lattice materials for high specific energy absorption under static and dynamic loading. *Acta Mater* **116**, 14–28 (2016).
30. He, Z. Z., Wang, F. C., Zhu, Y. B., Wu, H. A. & Park, H. S. Mechanical properties of copper octet-truss nanolattices. *J Mech Phys Solids* **101**, 133–149 (2017).
31. Qin, Z., Zhu, J., Li, W., Xia, Y. & Zhou, Q. System ringing in impact test triggered by upper-and-lower yield points of materials. *Int J Impact Eng* **108**, 295–302 (2017).
32. Schaedler, T. A. *et al.* Ultralight Metallic Microlattices. *Science (1979)* **334**, 962–965 (2011).
33. Cheng, H. *et al.* Mechanical metamaterials made of freestanding quasi-BCC nanolattices of gold and copper with ultra-high energy absorption capacity. *Nat Commun* **14**, (2023).
34. Bonatti, C. & Mohr, D. Large deformation response of additively-manufactured FCC metamaterials: From octet truss lattices towards continuous shell mesostructures. *Int J Plast* **92**, 122–147 (2017).
35. Mieszala, M. *et al.* Micromechanics of Amorphous Metal/Polymer Hybrid Structures with 3D Cellular Architectures: Size Effects, Buckling Behavior, and Energy Absorption Capability. *Small* **13**, (2017).
36. Zhang, X. *et al.* Three-Dimensional High-Entropy Alloy-Polymer Composite Nanolattices That Overcome the Strength-Recoverability Trade-off. *Nano Lett* **18**, 4247–4256 (2018).
37. Bauer, J., Schroer, A., Schwaiger, R. & Kraft, O. Approaching theoretical strength in glassy carbon nanolattices. *Nat Mater* **15**, 438–443 (2016).
38. Bauer, J., Hengsbach, S., Tesari, I., Schwaiger, R. & Kraft, O. High-strength cellular ceramic composites with 3D microarchitecture. *Proc Natl Acad Sci U S A* **111**, 2453–2458 (2014).
39. Malyar, N. V., Grabowski, B., Dehm, G. & Kirchlechner, C. Dislocation slip transmission through a coherent $S3\{111\}$ copper twin boundary: Strain rate sensitivity, activation volume and strength distribution function. *Acta Mater* **161**, 412–419 (2018).
40. Zhu, Y. T. *et al.* Dislocation–twin interactions in nanocrystalline fcc metals. *Acta Mater* **59**, 812–821 (2011).
41. Chassagne, M., Legros, M. & Rodney, D. Atomic-scale simulation of screw dislocation/coherent twin boundary interaction in Al, Au, Cu and Ni. *Acta Mater* **59**, 1456–1463 (2011).
42. Malyar, N. V., Micha, J. S., Dehm, G. & Kirchlechner, C. Dislocation-twin boundary interaction in small scale Cu bi-crystals loaded in different crystallographic directions. *Acta Mater* **129**, 91–97 (2017).

43. Wang, J. *et al.* Detwinning mechanisms for growth twins in face-centered cubic metals. *Acta Mater* **58**, 2262–2270 (2010).
44. Cao, Y. *et al.* Grain boundary formation by remnant dislocations from the de-twinning of thin nano-twins. *Scr Mater* **100**, 98–101 (2015).
45. Blewitt, T. H., Coltman, ; R R, Redman, ; J K, Coltman, R. R. & Redman, J. K. Low-Temperature Deformation of Copper Single Crystals. *J Appl Phys* **28**, 651–660 (1957).
46. Sarma, V. S. *et al.* Role of stacking fault energy in strengthening due to cryo-deformation of FCC metals. *Materials Science and Engineering: A* **527**, 7624–7630 (2010).
47. Ramachandramoorthy, R. *et al.* Anomalous high strain rate compressive behavior of additively manufactured copper micropillars. *Appl Mater Today* **27**, 101415 (2022).
48. Wei, Q., Cheng, S., Ramesh, K. T. & Ma, E. Effect of nanocrystalline and ultrafine grain sizes on the strain rate sensitivity and activation volume: fcc versus bcc metals. *Materials Science and Engineering: A* **381**, 71–79 (2004).
49. Wang, Y. M. & Ma, ; E. Temperature and strain rate effects on the strength and ductility of nanostructured copper. *Appl. Phys. Lett* **83**, 3165–3167 (2003).
50. Lu, L. *et al.* Nano-sized twins induce high rate sensitivity of flow stress in pure copper. *Acta Mater* **53**, 2169–2179 (2005).
51. Khantha, M., Vitek, V. & Pope, D. P. Strain-rate dependent mechanism of cooperative dislocation generation: application to the brittle–ductile transition. *Materials Science and Engineering: A* **319–321**, 484–489 (2001).
52. Jennings, A. T., Li, J. & Greer, J. R. Emergence of strain-rate sensitivity in Cu nanopillars: Transition from dislocation multiplication to dislocation nucleation. *Acta Mater* **59**, 5627–5637 (2011).
53. Mousavi Davoudi, S. A. & Naghipour, M. Presentation of Critical Buckling Load Correction Factor of AISC Code on L-Shaped Composite Columns by Numerical and Experimental Analysis. *International Journal of Steel Structures* **20**, 1682–1702 (2020).
54. Lee, A., Jiménez, F. L., Marthelot, J., Hutchinson, J. W. & Reis, P. M. The Geometric Role of Precisely Engineered Imperfections on the Critical Buckling Load of Spherical Elastic Shells. *Journal of Applied Mechanics, Transactions ASME* **83**, (2016).
55. Ranjbartoreh, A. R. & Wang, G. Effect of Topological Defects on Buckling Behavior of Single-walled Carbon Nanotube. *Nanoscale Res Lett* **6:28**, (2010).

56. Ercolano, G. *et al.* Additive manufacturing of sub-micron to sub-mm Metal structures with hollow AFM cantilevers. *Micromachines (Basel)* **11**, (2020).
57. Zhang, S. & Scheu, C. Evaluation of EELS spectrum imaging data by spectral components and factors from multivariate analysis. *Microscopy* **67**, i133–i141 (2018).
58. Wheeler, J. M., Armstrong, D. E. J., Heinz, W. & Schwaiger, R. High temperature nanoindentation: The state of the art and future challenges. *Curr Opin Solid State Mater Sci* **19**, 354–366 (2015).

Figure 1. Pure Cu microlattices and their structural and microstructural analysis. (a) Cu microarchitectures fabricated by localized electrodeposition process. (b) Computer-aided design of microlattice. (c) Voxel locations of microlattice. (d) SEM image of as-fabricated Cu microlattice. (e) Reconstructed microlattice and unit-cell by NanoCT. (f) Strut diameter distribution of as-fabricated microlattice. (g and h) Inverse pole figure map and grain boundary map of representative unit cross-section of microlattice obtained using TKD.

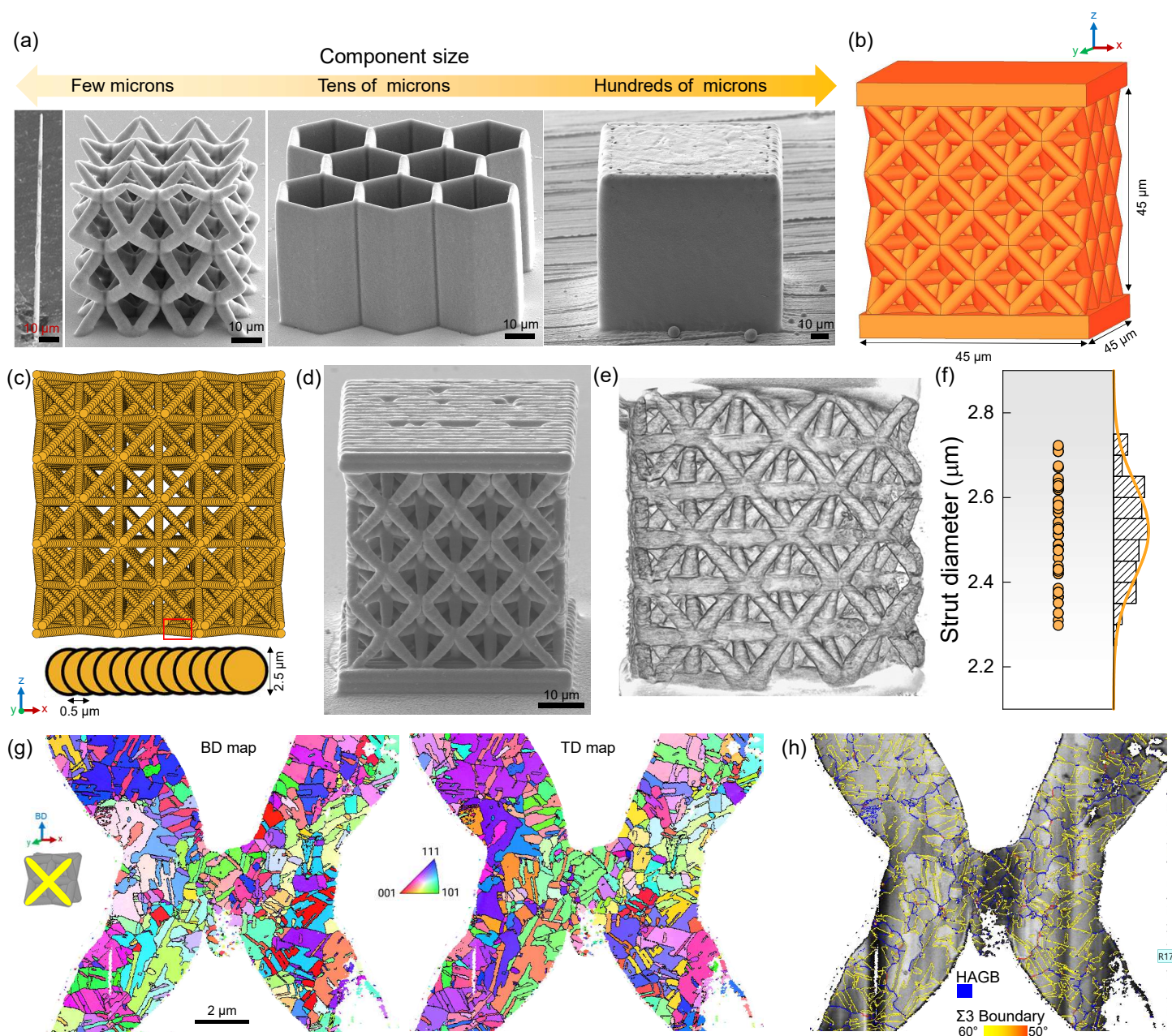


Figure 2. Compression test of micro-lattice. (a and b) SEM images of microlattices during compression at RT and CT, respectively at a strain rate of 0.01 s⁻¹. (c) Engineering stress-strain curves of microlattices compressed at various temperatures and strain rates (Zoomed in inset: Representative stress-strain curves for RT and CT upto strain rates of 0.1/s). (d) Yield strengths of microlattices. (e and f) SEM images of compressed microlattices. (g) Comparison of absorbed energy of microlattice with previously reported values.

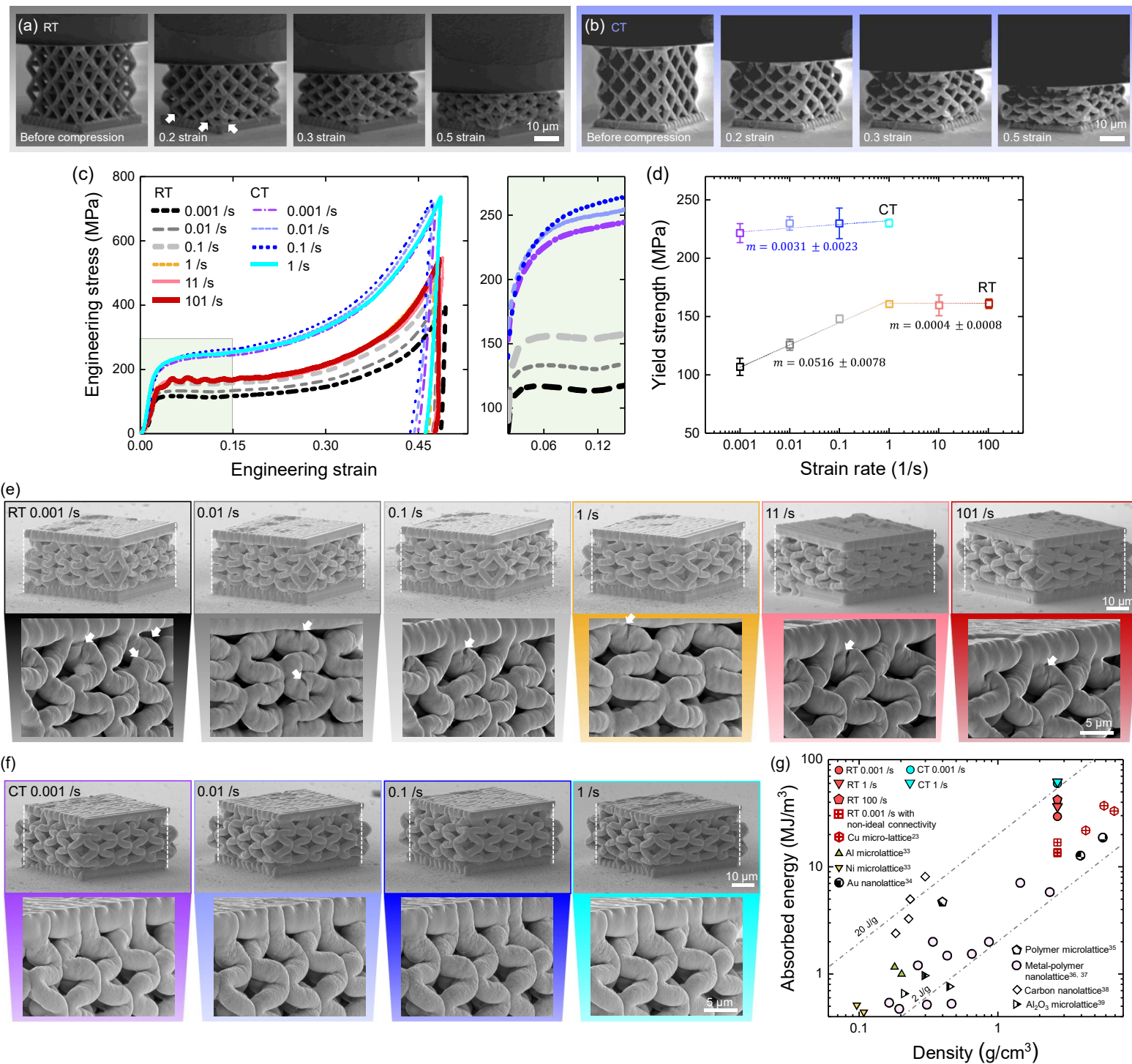


Figure 3. Cu micropillars and Compression test. (a) Computer-aided design of micropillar. (b) Voxel locations of micropillar. (c) SEM images of micropillars. White box indicate a region of interest for cross-sectional microstructure analysis (d) Inverse pole figure map and grain boundary map of cross-section of micropillar obtained using TKD. (e) Engineering stress-strain curves of micropillars compressed at various temperatures and strain rates. (f) Yield strengths of micropillars. (g) SEM images of compressed micropillars.

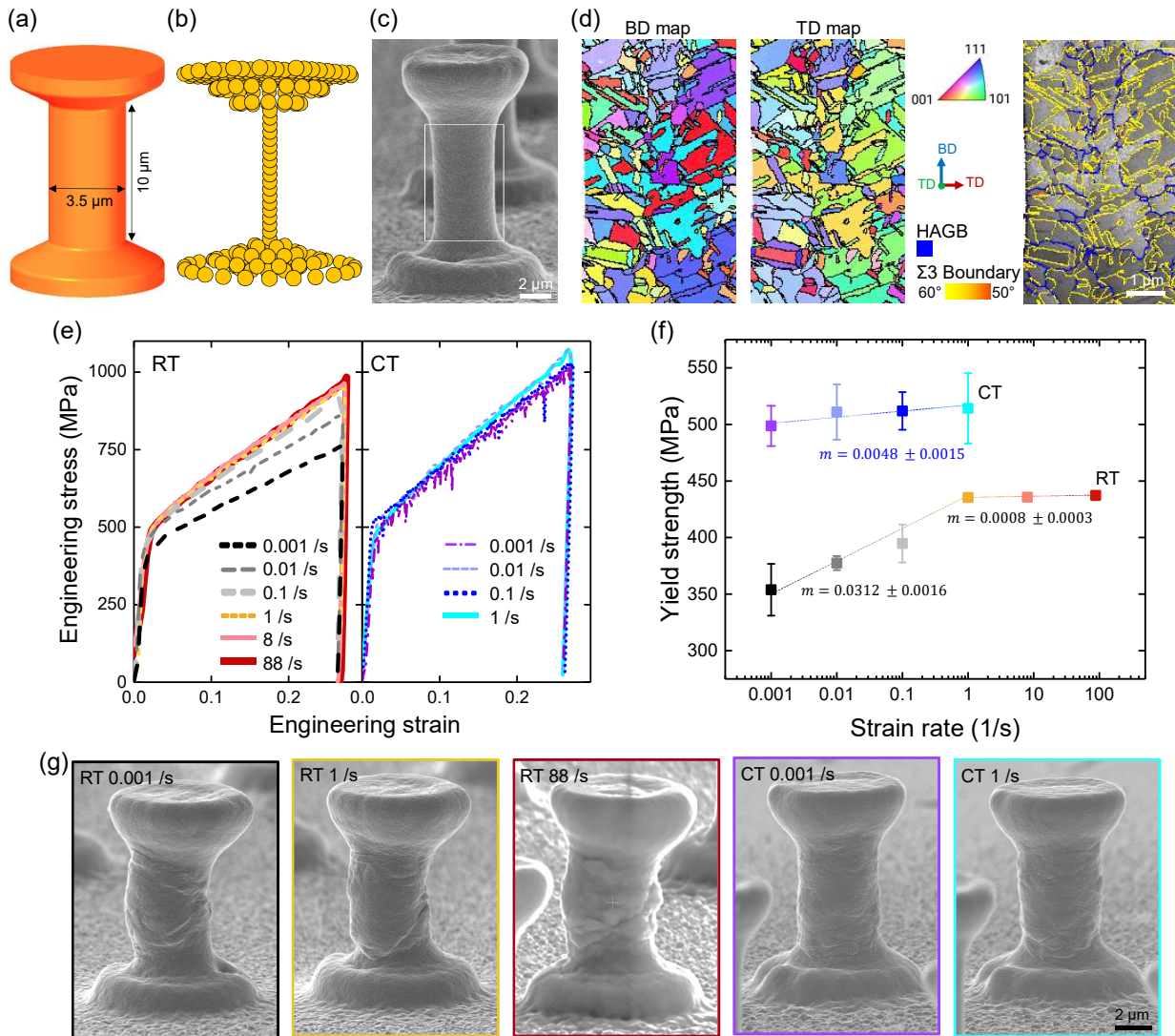


Figure 4. Deformation mechanism of copper micropillars. (a and b) Inverse pole figure map and grain boundary map of cross-section of compressed micropillar. (c) HAADF-STEM image and FFT patterns obtained from atomically resolved areas with straight twin boundaries in micropillar compressed at CT 0.001 /s. (d) Misorientation angle distribution of micropillar without compression (top), compressed at 0.001 /s (middle) and compressed at 1 /s (bottom). (e) Stress drop magnitude with respect to drop time obtained from stress-strain curves of micropillars compressed at CT 0.001, 0.01, and 0.1 /s. Inset is engineering stress-time plot of micropillar compressed at CT 0.01 /s. (f) Schematics of postulated deformation mechanism in copper micropillar.

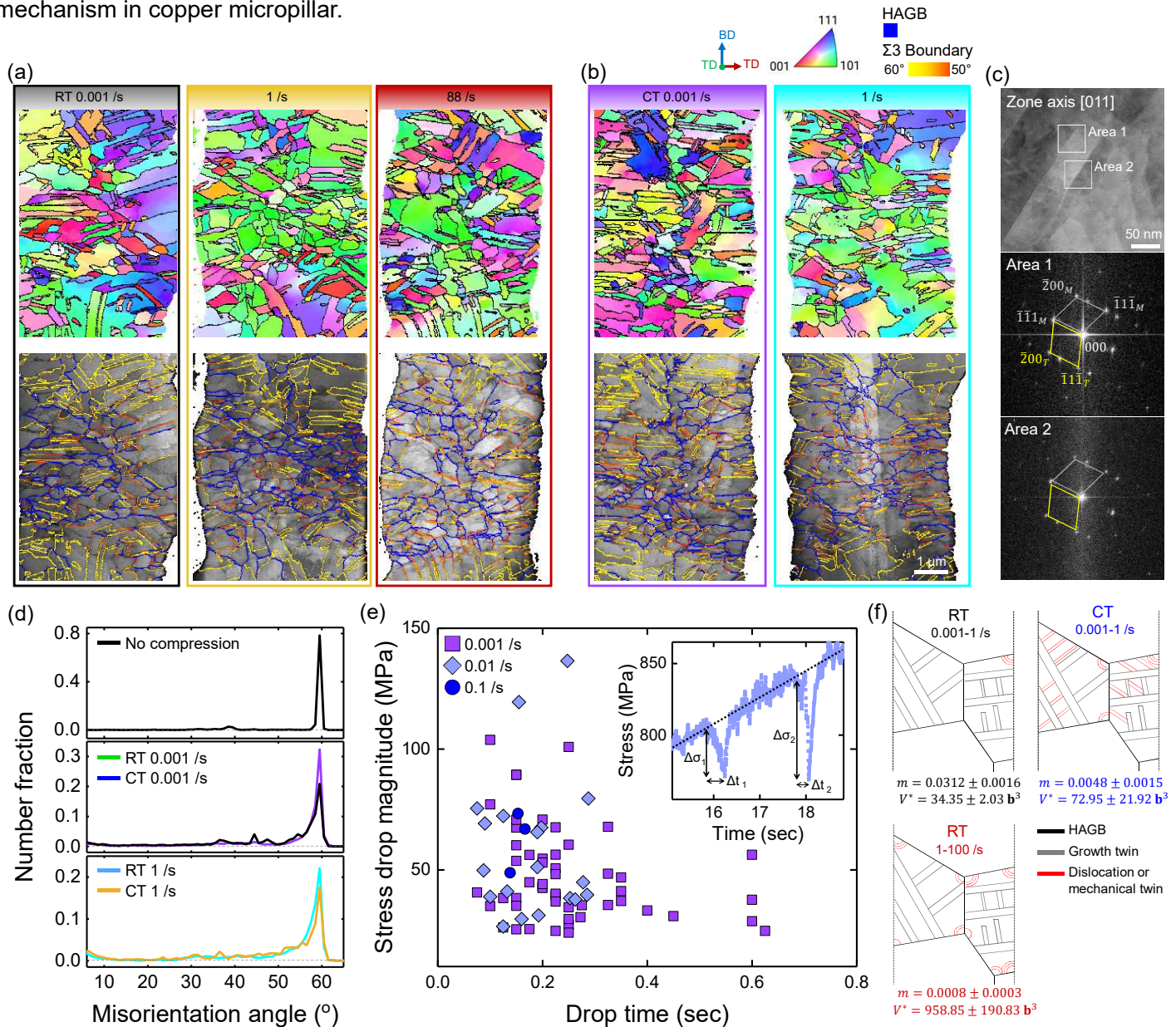


Figure S1. SEM images of Cu microlattices fabricated with different printing overpotentials at the same pressure of 20mbar (Scale bars : 10 μ m).

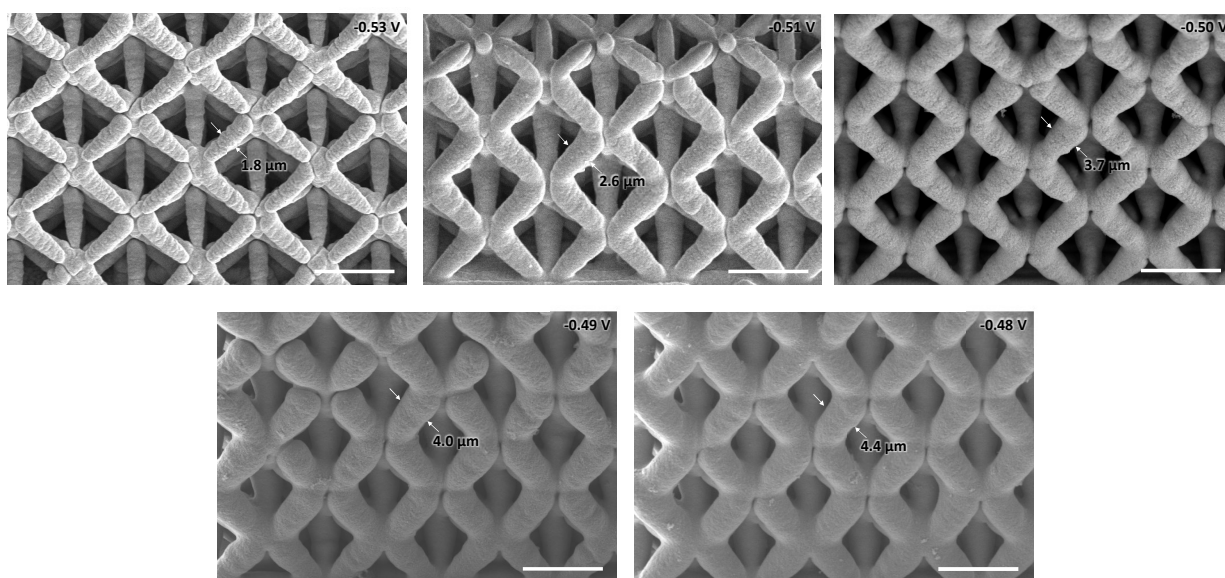


Figure S2. Flow stress (at 0.2 engineering strain) of microlattices at different temperatures and strain rate conditions.

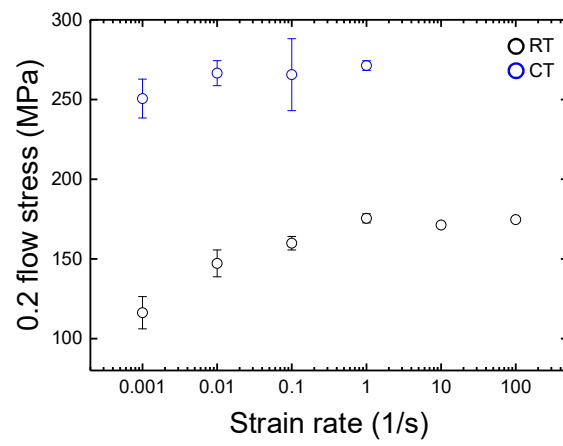


Figure S3. Stress-strain curves of microlattices. (a) At RT and 0.001, 0.01, 0.1, 1, 10 s⁻¹. (b) At CT and 0.001, 0.01, 0.1, 1 s⁻¹.

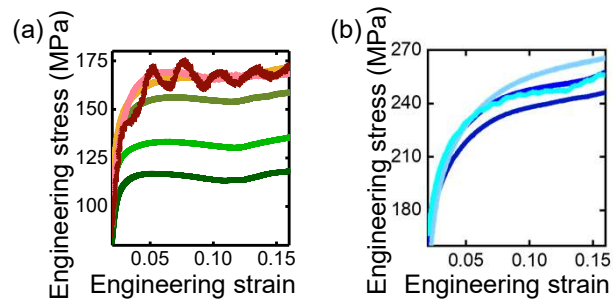


Figure S4. Degree of bulging out of compressed microlattices.

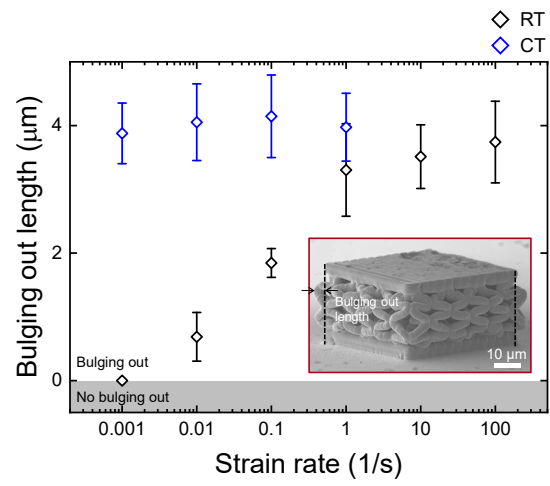


Figure S5. Deformation behavior of LELed pure Cu micro-lattices with poor nodal connectivity.

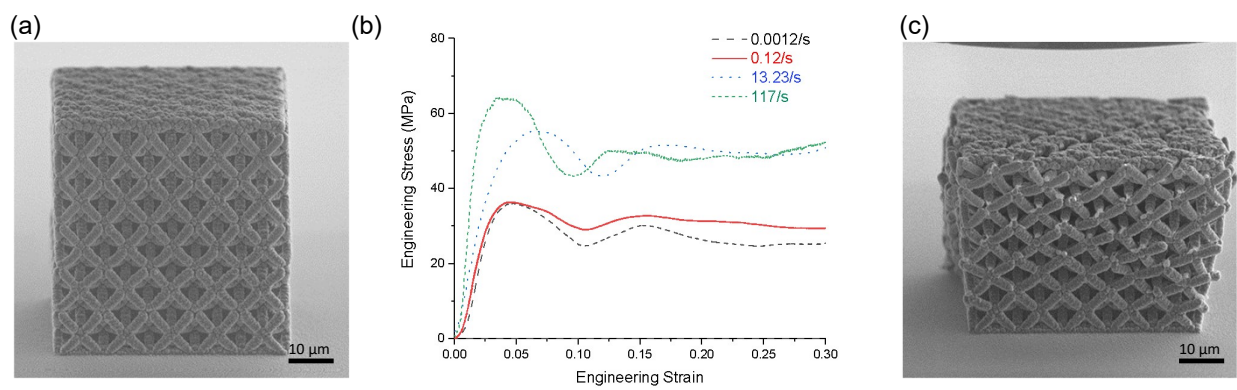


Figure S6. Finite element analysis of (a) Calculated compressive load-displacement curves of microlattices with and without top plate. (b) Plastic strain distribution in microlattices.

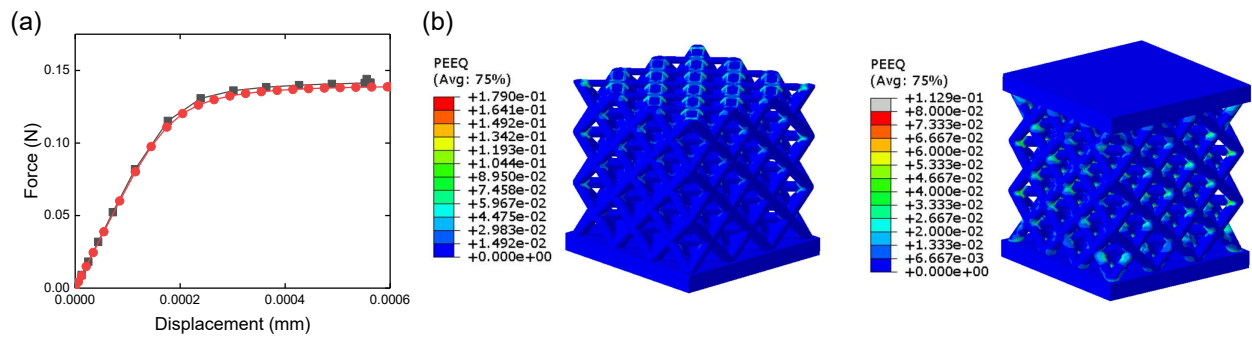


Figure S7. Strain rate map of microlattice cross-section calculated by FE simulation.

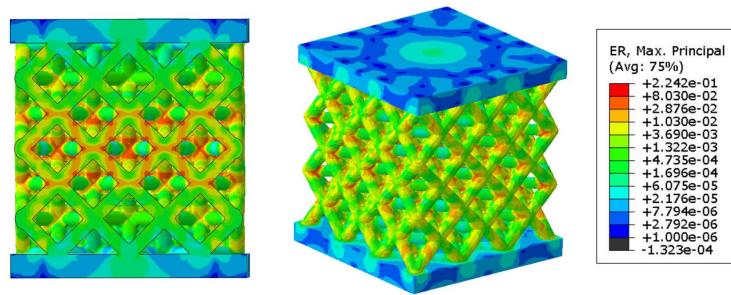


Figure S8. Misorientation angle distribution of microlattice and micropillar.

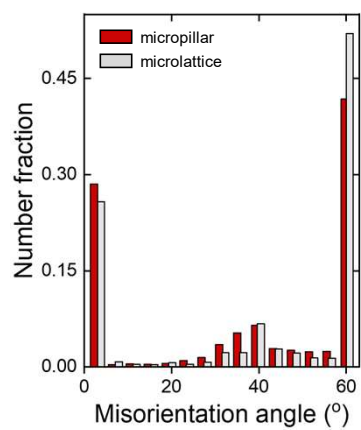


Figure S9. Flow stress (at 0.2 engineering strain) of micropillars at different temperatures and strain rate conditions.

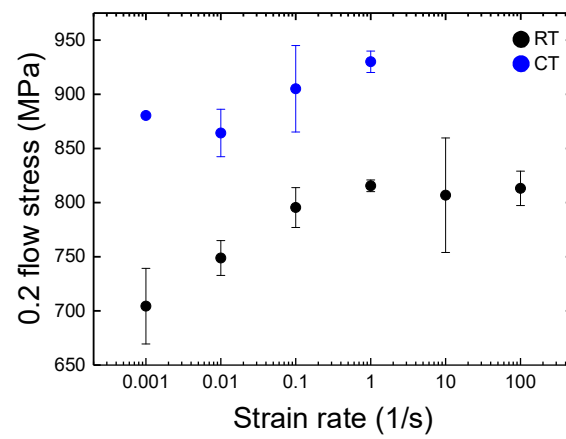


Figure S10. SEM images of compressed micropillars.

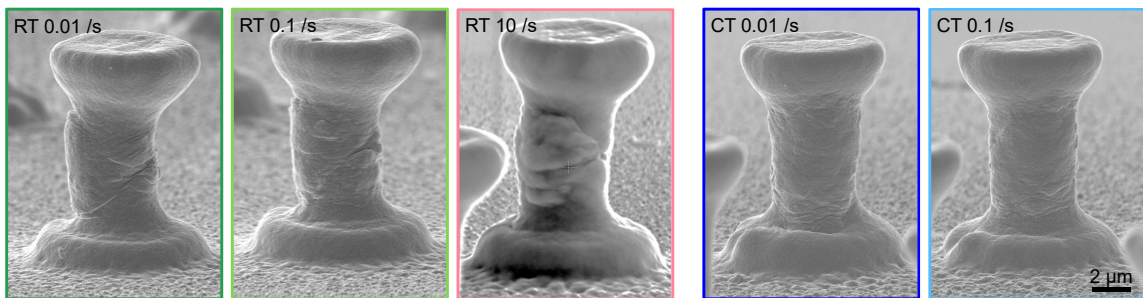


Figure S11. Grain boundary maps and corresponding pole figure maps of micropillar compressed at CT 0.001/s.

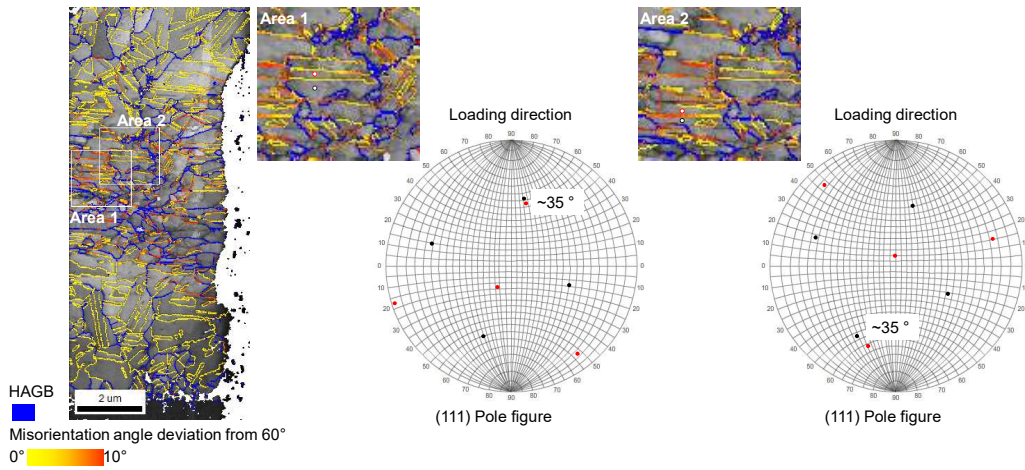


Figure S12. Hardening modulus of micropillars – Cryogenic temperature – blue circles and room temperature – black circles.

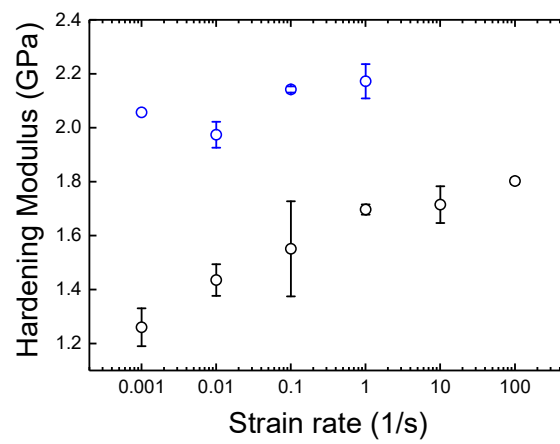


Figure S13. Dynamic increase factor of microlattices (empty squares) and micropillars (solid squares).

